Holographic fabrication of three-dimensional nanostructures for microfluidic passive mixing†

Sung-Gyu Park,[a] Seung-Kon Lee,[a] Jun Hyuk Moon[b] and Seung-Man Yang*[a]

Received 10th July 2009, Accepted 31st July 2009
First published as an Advance Article on the web 21st August 2009
DOI: 10.1039/b913817j

In this study, we incorporated mixing units of three-dimensional (3D) interconnected pore network inside microfluidic channels by combining single prism holographic lithography and photolithography. 3D pore network structures were generated by the interference of four laser beams generated by a truncated triangular pyramidal prism. The levelling between the 3D porous structures and the channel walls was greatly improved by employing supercritical drying, which induced negligible internal capillary stresses and reduced substantially anisotropic volume shrinkage of 3D structures. Also, complete sealing of the microfluidic chips was achieved by attaching flexible PDMS cover substrates. Overall mixing performance of the systems with completely sealed mixing units was 84% greater than that obtained without such mixers. Splitting and recombination of flows in the 3D interconnected pore structures enhanced the mixing efficiency by decreasing the diffusion path and increasing the surface contact between two liquid streams. Because the flow splitting and recombination was developed through the 3D interconnected pore network, high mixing efficiency (>0.60) was achieved at low Reynolds numbers ($Re < 0.05$) and Péclet numbers in the regime of $Pe < 1.4 \times 10^3$.

Introduction

Microfluidic devices have been widely applied in chemical and biological systems because they enable high-throughput, precise processes with minimal consumption of reagents. Since the manipulation of fluids is an important concern, extensive research has been performed on the integration of various microdevices including micropumps, micromixers, and microreactors. Mixing within microfluidic devices has been a challenging area of research because flow within microchannels is characterized by low Reynolds numbers ($Re < 1$). Here, Re is defined by $Re = l_c U\rho/\mu$ in which l_c and U are the characteristic length and velocity of the flow, respectively, and ρ and μ are the density and viscosity of the fluid, respectively. Therefore, only diffusion can contribute to the mixing process.

The mixers for microfluidic devices can be classified into passive and active types. Active micromixers rely on actuations by some external means including pressure, electrohydrodynamics, acoustics, or dielectrophoresis.[1] While mixing can be achieved more efficiently by active mixers, the fabrication of these mixers often requires extensive processing and external operating devices. Passive mixers, by contrast, use unique channel designs in order to enhance distributive mixing,[2–5] chaotic advection,[6–9] or laminar shear.[10] A useful strategy is the incorporation of 3D pores that provide highly compact substream channels and enhance the mixing efficiency even at low Re. The geometry of 3D porous structures can split two inlet streams into multiple substreams and then recombine them at the outlet. In this way, the interconnected pore network increases the contact surface between the two fluids and thereby decreases the required diffusion length (or time) for the complete mixing. For example, direct patterning using a phase-mask showed a simple, well-defined design of 3D structures in microfluidic channels[11,12] and the interstices between colloidal beads packed within microchannels were able to increase the mixing rate.[13] Recently, porous polymer monoliths (PPM) were integrated in a microfluidic device by using *in situ* UV irradiation through a mask.[14] The photopatterned PPM enhanced the mixing and overall rate of chemical reaction in the system.

Herein, we demonstrated a simple and new strategy for 3D structured mixers in microfluidic chips that combines multi-beam holographic lithography[15–18] and photolithography. We used a truncated triangular pyramidal prism to generate 3D porous structures by four beam interference patterns.[17] Three beams are generated by refraction from the three side surfaces of the prism and a central beam travels through the top truncated surface of the prism. These four beams recombine at the bottom of the prism, which sits on the top of a SU-8 photoresist (PR) layer, which allows for sequential patterning of the channel and the 3D pore network. Compared to the phase-mask approach, holographic lithography is able to control the properties of the interfering beams, which enables various designs of 3D interconnecting pore network uniformly throughout the micromixers.[18] In general, however, the 3D structures of photoresist tend to shrink substantially during the lithographic fabrication and anisotropic shrinkage occurs when the 3D structures are pinned to the microchannel walls. To utilize the 3D structures as

[a]*National Creative Research Initiative Center for Integrated Optofluidic Systems and Department of Chemical and Biomolecular Engineering, KAIST, Daejeon, 305-701, Korea. E-mail: smyang@kaist.ac.kr; Fax: +82-42-350-5962; Tel: +82-42-350-3922*
[b]*Department of Chemical & Biomolecular Engineering, Sogang University, 1 Shinsu-dong, Mapo-gu, Seoul, 121-742, Korea*

† Electronic supplementary information (ESI) available: Contact angle measurement data, and OM images of the breakage of a microfluidic chip and an SEM image of a lower void fraction of 3D structures. See DOI: 10.1039/b913817j

passive mixers, we further studied to resolve the volume shrinkage problem, which facilitated the levelling of 3D mixer against the channel height during exposure and development steps. This is a crucial step to fit the 3D mixers in the microchannel without generating by-pass flow. The volume shrinkage was greatly improved by supercritical drying, which exerted negligible capillary force and reduced internal stress within 3D polymeric pore network. Finally, mixing of two aqueous liquids has been tested to demonstrate the enhanced mixing efficiency of the 3D mixers.

Experimental

A. Fabrication of microfluidic chips

A typical procedure for fabricating a 3D mixer in a microfluidic channel is shown in Fig. 1. The PR was composed of epoxy-based resin (EPON SU-8, Miller-Stephenson Chemical), cationic photoinitiator (PI, triarylsulfonium hexafluorophosphate salts, Dow Chemicals) and solvent (gamma-butyrolactone (GBL), Sigma-Aldrich). The PR for the microfluidic chip was also formulated by mixing SU-8 resin (150 wt% to solvent) and PI (1.3 wt% to resin) in GBL. A 14.4 μm thick PR layer was obtained by spin casting the PR solution onto a glass substrate and subsequently soft-baking at 95 °C for 20 min to evaporate the solvent. The layout of the microfluidic channel was defined by exposing the sample to 365 nm UV light through a Y-junction positive photomask (Fig. 1a). Next, a laser beam (HeCd laser, CW, 325 nm, 50 mW, Kimmon, beam diameter = 1 cm) was passed through a beam expander and then directed perpendicularly to a top-cut fused silica prism with a refractive index of 1.48 at 325 nm (Fig. 1b). It is important to note that the SU-8 PR is sensitive to both the 325 nm HeCd laser source and the 365 nm Hg lamp source. The optical setup and geometric features of the prism were previously reported.[17] During laser exposure, a 2 mm wide transparent slit was placed on the SU-8 PR to define the length of the 3D mixers. The post-exposure bake was performed at 55 °C for 20 min to minimize the internal stress within the 3D polymer network. After developing the sample with propylene glycol methyl ether acetate (PGMEA) and rinsing with H_2O (Fig. 1c), the narrower pores in the overexposed region was enlarged by reactive-ion etching (RIE, Vacuum Science) with a composition of CF_4:O_2 = 20:200 sccm for 45 min to facilitate the fluid flow through the mixer unit. The base pressure was kept at 0.13 torr while the RF power was maintained at 100 W. Instead of rinsing with H_2O, isopropanol was dried out from the sample by using supercritical carbon dioxide, which enhanced the structural integrity of the 3D porous structures. During the RIE process, the unpatterned regions of the sample were covered by a thin, PDMS etching mask. The sample was treated with 0.2 M H_2SO_4 for 30 min to make the mixer hydrophilic. The H_2SO_4 treatment reduced the contact angle of the 3D pore network structures from 114° to 25°. The contact angle measurement data are included in Fig. S1 of the ESI†. In the final step, the SU-8 mixers and channel were glued to the deformable PDMS substrate (Fig. 1d). The combined chips were then annealed at 70 °C in a convection oven for 1 h to ensure chemical bonding.

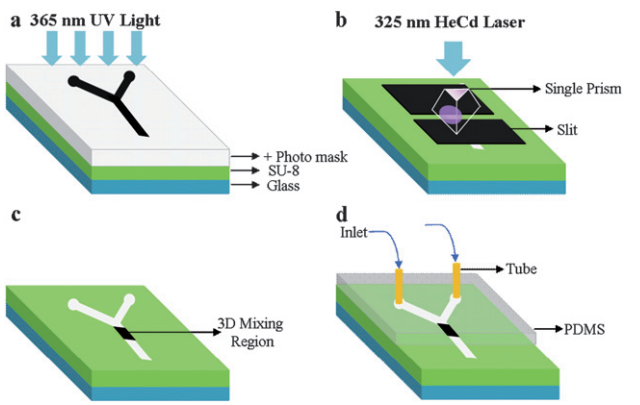

Fig. 1 Schematic illustration of the typical procedure for fabricating a 3D mixer in a microfluidic channel. (a) UV exposure through a Y-shaped positive photomask. (b) Holographic lithography using a single refracting triangular prism. (c) Post-exposure bake and development. (d) Bonding a flexible PDMS cover to a SU-8/glass substrate.

B. Characterizations

Surface and cross-sectional images of the samples were captured using a field emission-scanning electron microscope (FE-SEM, Hitachi S-4800). The reflectance spectra of the sample were analyzed by FT-IR and imaging microscopy (IFS 66v/s & HYPERION™ 3000, Bruker) with a 15 × IR objective lens; the spot size was 100 μm × 200 μm.

3D porous structures featured by holographic lithography have photonic band-gaps (PBGs) due to their structural periodicity for light propagating in the [111] direction. The PBG can be characterized by the reflectance spectra for normal incident light onto the [111] plane. The location of the reflectance peak or PBG can be expressed by Bragg's law:

$$\lambda = 2d_{111}n_e \quad (1)$$

in which λ is the peak wavelength of reflectance, d_{111} is the interlayer distance in the [111] direction. The effective refractive index n_e is simply estimated as:

$$n_e = \sqrt{fn_f^2 + (1-f)} \quad (2)$$

Here, n_f represents the refractive index of the skeleton material (*i.e.*, SU-8) and $(1 - f)$ is the void fraction of the 3D porous structures.

The mixing efficiency was evaluated using the fluorescence technique. During testing, one syringe was filled with an aqueous Rhodamine 6G (R6G) solution (10^{-4} M) while the other was filled with pure water. Using syringe pumps (KD Scientific Inc., Holliston, MA), the two syringes were driven at flow rates between 2 μl/hr and 60 μl/hr, corresponding to mean velocities between 0.4 mm/s and 11.6 mm/s. Devices were imaged on a Zeiss LSM510 laser scanning confocal microscope (Carl Zeiss Inc.) using a 543 nm HeNe laser and a 5× Plan-Neofluar objective and a 78 μm pinhole, for a pixel resolution of 1.8 μm × 1.8 μm × 1.0 μm. The fluorescence intensities I_U and I_L were measured at the respective regions along a single line located at either the inlet or the outlet of the mixer unit. We calculated the mixing efficiency by integrating the fluorescence intensities of the upper and

lower regions in the microchannel. To get accurate values, we took three different single lines for scanning the intensities at both ends and estimated the mixing efficiencies by averaging the three integrated intensities. To estimate the mixing efficiency, the relative fluorescence intensity ε of the lower part (which was occupied originally by pure water at the upstream of the mixer) was calculated with respect to the average integrated intensity.

$$\varepsilon = \frac{2\bar{I}_L}{\bar{I}_U + \bar{I}_L} \quad (3)$$

Here, $\bar{I}_U$ and $\bar{I}_L$ represent the integrated intensities in the upper and lower regions, respectively. Then, the mixing efficiency E_{mixing} is defined as:

$$E_{mixing} = \frac{\varepsilon_{out} - \varepsilon_{in}}{1 - \varepsilon_{in}} \quad (4)$$

where ε_{in} and ε_{out} are the relative intensities at the lower half-regions of the inlet and outlet of the mixer, respectively.[12] Therefore, the mixing efficiency E_{mixing} represents the normalized intensity enhancement at the lower part relative to the value for the perfect mixing case. We estimated the mixing efficiency from Eqn. (4) for two different lengths of 3D mixing units, $l = 1.2$ mm and 1.5 mm.

Results and discussion

A. Incorporation of 3D porous structures inside a microfluidic channel

Scanning electron microscope (SEM) images in Fig. 2 show a typical microfluidic passive mixer with 3D interconnected pores. In this system, the microchannel was 100 μm wide and 14.4 μm high and contained a mixing unit of 3D pore network. The SEM images in Fig. 2b and 2c show that our 3D mixers possess interconnected pores that are arranged into a face-centered cubic (FCC) lattice with a lattice constant of 650 nm. Meanwhile, we found the overexposure near the edge of the slit by diffraction, resulting in a locally lower void fraction of 3D structures and breakage of the microfluidic chip. Optical microscope (OM) images of the breakage and an SEM image of 3D structures with a lower void fraction are available in the ESI† (Fig. S2). To facilitate the inlet and outlet flows, RIE was applied to the entrance and exit regions of the 3D mixers.

The void fraction and pore size in the 3D pore network structures were controlled by adjusting the laser dose, post-exposure bake temperature, and rinsing solvent. Figs. 3a–3d show cross-sectional SEM images of 3D mixing units fabricated under various process conditions. Also included in Fig. 3e are the reflectance spectra of the samples prepared at different conditions. The pore size becomes smaller and the reflectance peak (or photonic bandgap) is redshifted as the exposure dose increases (Fig. 3 and Table 1). The average lattice spacings (d_{111}) of the 3D structure were increased up to 780 nm from 700 nm by

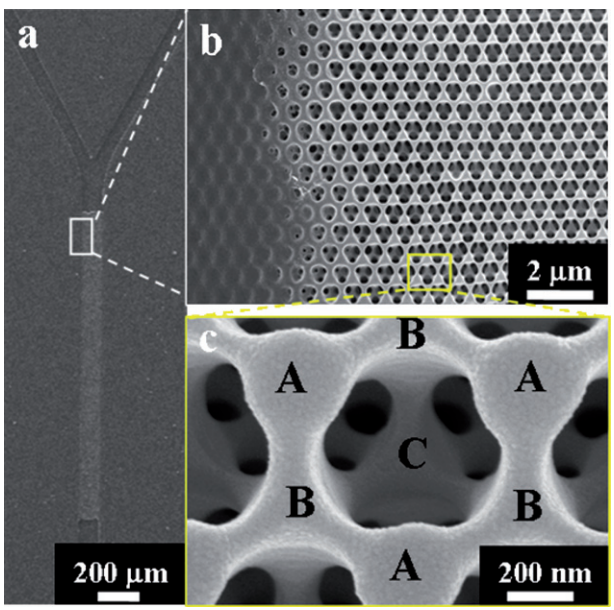

Fig. 2 Structure of a 3D microfluidic passive mixer fabricated by holographic lithography and photolithography. (a) Scanning electron microscope (SEM) image of the Y-shaped channel with a 3D mixing unit. (b) High resolution SEM image of the boundary between 3D porous structures and the channel wall. (c) Magnified SEM image of 3D pore structure with FCC symmetry. A, B and C represent the three repeated stacking layers of FCC structure. The lattice constant is 650 nm.

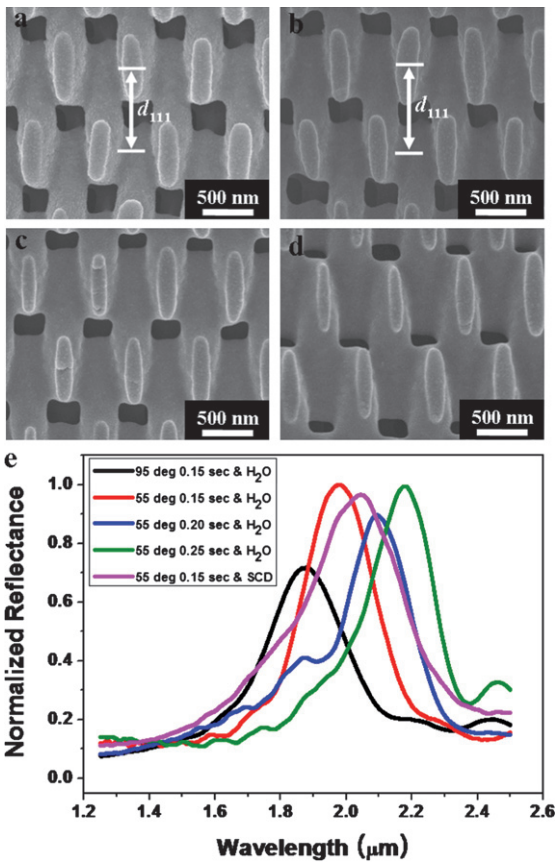

Fig. 3 Control of the void fraction and pore size by varying process conditions. Cross-sectional SEM images of 3D mixing units with (a) rinsing with H_2O and with (b) supercritical drying (SCD) for an exposure time of 0.15 s and a post-exposure bake temperature of 55 °C. Cross-sectional SEM images of 3D mixing units with exposure times of (c) 0.20 and (d) 0.25 s when the post-exposure bake temperature is 55 °C and rinsing solvent is H_2O. (e) Reflectance spectra of the 3D structures obtained using various process conditions.

Table 1 Variation of the void fractions according to the process conditions

Experimental condition					
Expo. time (s)	PEB temp. (°C)	Rinsing	Interlayer distance (nm)	Reflectance peak (μm)	Void fraction
0.15	95	H_2O	700	1.90	0.44
	55	H_2O	750	1.98	0.50
	55	SCD	780	2.04	0.52
0.20	55	H_2O	760	2.09	0.40
0.25	55	H_2O	768	2.18	0.31

applying supercritical drying and reducing the post-exposure bake temperature. Consequently, the void fraction was increased from 0.44 to 0.52 (Fig. 3b and Table 1).

B. Reduction of anisotropic volume shrinkage of 3D porous structures

Another important issue on the fabrication was large volume shrinkage of 3D structures compared to the channel walls. Extensive shrinkage must be avoided in order to allow for complete sealing within the device. With incomplete sealing, an undesirable leak occurs between the 3D structures and PDMS substrate (Fig. 4a), which deteriorates the mixing efficiency substantially. Shrinkage of the 3D porous structures results from capillary forces that are present during the development and drying steps. Additional shrinkage may occur with negative photoresists which experience a free volume reduction during crosslinking of the polymer network. Therefore, we lowered the post-exposure bake temperature to reduce the internal stress in the 3D porous structures and applied rinsing solvents that induce smaller capillary forces.[19,20] We lowered the post-exposure bake temperature to 55 °C instead of the typical temperature of 95 °C, which was the lowest temperature but sufficiently enough to sustain the structure in a developing solvent. In addition, the sample was treated with water after rinsing with isopropanol. In this case, the capillary force exerted by water is approximately 50% lower than that exerted by isopropanol.[21] The thickness of 3D mixer scaled by the height of channel wall was greatly increased from 0.69 to 0.81 under the optimized conditions as shown in Fig. 4a and 4b. Finally, we applied supercritical drying to further reduce the volume shrinkage within the device. In a supercritical liquid, the surface tension becomes negligible and the capillary force is trivially small.[20] The normalized height of the 3D mixer was further increased to 0.85. The residual gap in Fig. 4c can be further reduced by attaching a flexible PDMS cover substrate.

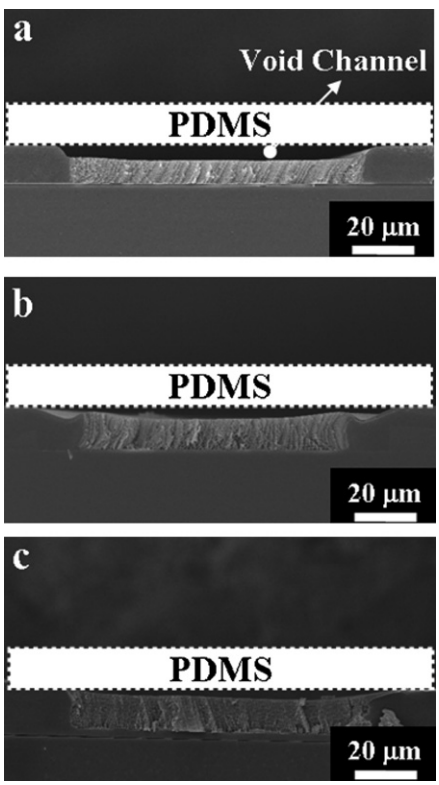

Fig. 4 Anisotropic volume shrinkage between the 3D porous structures and the channel wall. (a) Cross-sectional SEM image of the 3D pore structure and the channel wall after post-exposure bake at 95 °C for 8 min and rinsing with isopropanol. (b) Cross-sectional SEM image of the 3D structure and the channel wall after post-exposure bake at 55 °C for 20 min and rinsing with H_2O. (c) Cross-sectional SEM image of the 3D structure and the channel wall after post-exposure bake at 55 °C for 20 min and drying with supercritical liquid CO_2. The minimum heights of (a), (b) and (c) normalized by the wall height are 0.69, 0.81 and 0.85, respectively.

C. Pressure drop across 3D micromixers

The average flow velocity U along a conduit of rectangular cross-section with width (w) and height (h) is approximately

$$U \approx \frac{h^2 \Delta p}{12 \mu L}\left[1 - 0.630\frac{h}{w}\right], \quad \text{for } w > h \tag{5}$$

in laminar Poiseuille flow regime.[22] Here, Δp is the pressure drop along the liquid path, μ is the fluid viscosity and L is the channel length. Eqn. (5) for U is surprisingly good. The worst case is for a square conduit with $h = w$, and the largest error was reported to be just 13%. However, at an aspect ratio of a half, $h = w/2$, the error is dropped to 0.2%.[22] Rearranging Eqn. (5) for our channel geometry ($h/w = 0.144$), we obtain

$$\frac{\Delta p}{L} \approx 1.10 \cdot \frac{12 U \mu}{h^2} \tag{6}$$

This equation confirms that the pressure drop per unit length is directly proportional to the flow velocity. The average flow velocity (U) was calculated from the volumetric flow rate (Q, μL/min), and the cross-sectional area of the channel ($w \times h = 100\ \mu m \times 14.4\ \mu m$). The flow velocity ($U_{in} = U/(1 - f)$)

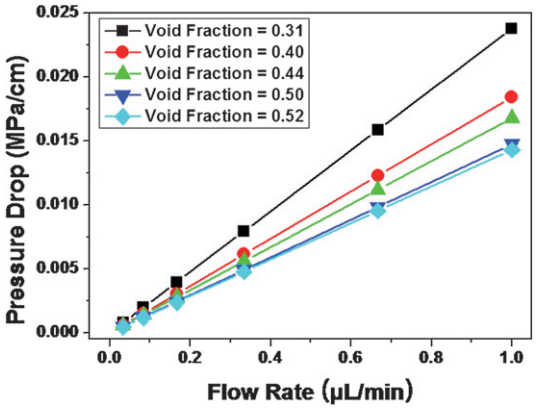

Fig. 5 Calculated pressure drop per unit length of 3D micromixer with different void fractions.

in the 3D mixing unit was determined by the average flow velocity and the void fraction $(1 - f)$ of the pore structure. Therefore, the pressure drop across the straight mixer is

$$\frac{\Delta p}{L} \approx 1.10 \cdot \frac{12\mu}{h^2} \cdot \frac{U}{(1-f)} \tag{7}$$

Eqn. (7) indicates that the pressure drop per unit length is inversely proportional to the void fraction. Fig. 5 presents the calculated pressure drop per unit length induced by 3D mixers with different void fractions. The pressure drop per unit length of the mixer with void fraction of 0.52 at flow rate of 1 μL/min was 0.015 MPa/cm, which was comparable to that of porous polymer monoliths with median pore diameter of 10.7 μm and porosity of 50%.[23]

D. Mixing efficiency of 3D micromixer

We used 3D pore network structures to test the mixing of two aqueous streams from the Y-shaped channels. Fig. 6a displays a confocal microscopy image of a completely sealed 3D mixer at a flow velocity of 1.0 mm/s. An aqueous Rhodamine 6G (R6G) solution of 10^{-4} M was forced to flow in the upper portion ($0 < x < 50$ μm) while pure water was flowing in the lower portion (50 μm $< x <$ 100 μm) of the channel with lateral dimension of 100 μm. Interestingly, we observed no fluorescence in the middle of the 3D mixing region, as shown in Fig 6a. This is due to the complete fit of the 3D mixer in the microchannel, which prevents by-pass flow between the 3D mixer and the flexible PDMS cover substrate. The volume shrinkage of 3D structures was minimized by the low temperature post-exposure bake and the use of supercritical drying, and the residual gap between the top of the 3D micromixing unit and the PDMS cover was greatly reduced by the flexible nature of the PDMS substrate. Fig. 6b and 6c show the line scans of the fluorescence intensities from confocal microscopy across the channel at the outlet and inlet regions of the mixer unit. In these intensity plots, I_U and I_L are the fluorescence intensities of the upper and lower half-regions of the 100 μm wide channel. We calculated the mixing efficiency from Eqns. (3) and (4). For the example case of Fig. 6, the mixing efficiency of 3D mixer with complete sealing was measured to be 0.59 ± 0.04; for "no mixer" system with the same channel geometry, it was 0.35 ± 0.01.

Fig. 7a shows the mixing efficiencies of 3D mixers as a function of the flow velocity for two different lengths of the mixing unit, $l = 1.2$ and 1.5 mm. Also included for comparison is the mixing efficiency of the "no mixer" system for $l = 1.2$ mm. As noted, the mixing efficiencies as a function of the flow velocity fitted into straight lines in log-log scale plots. In the "no mixer" system, the mixing was driven purely by diffusion and the efficiency was proportional to −1/2 power (−0.50 ± 0.02) of U. Indeed, the power law was consistent with theoretical scaling law in pressure-driven laminar flows.[24,25] For a microchannel of width $w = 100$ μm without a mixer, the fluids required the diffusion time ($\tau \sim w^2/4D$) of 9 s and the mixing length ($\sim \tau U$) of 17 mm to be mixed uniformly at the flow velocity (U) of 1.9 mm/s, where the diffusion coefficient $D = 2.8 \times 10^{-10}$ m^2/s. However, the flow splitting and recombination in the 3D interconnected pore network reduced substantially the required diffusion time and mixing length for the diffusive mixing. Consequently, the mixing

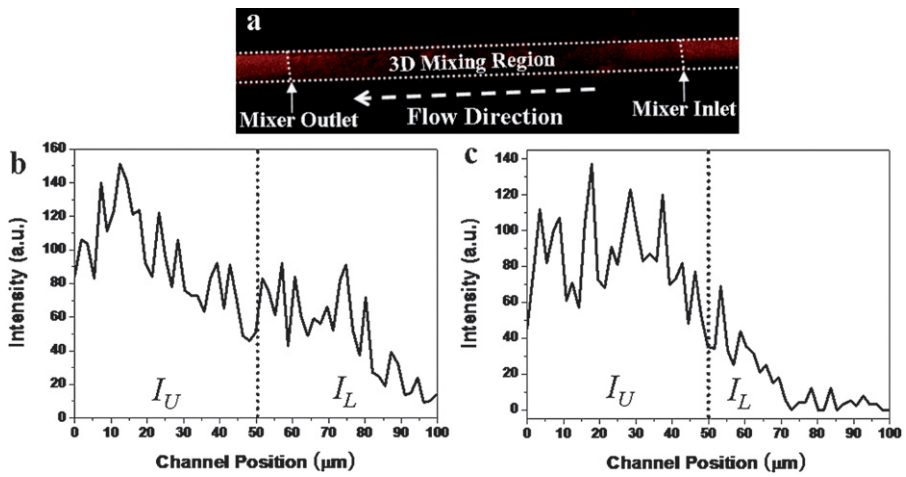

Fig. 6 Mixing efficiency. (a) Confocal microscopy image of a completely sealed 3D mixer with flexible PDMS cover at a flow velocity of 1.0 mm/s. The fluorescence intensities (b) at the outlet and (c) at the inlet of the 3D mixer when the flow velocity is 1.0 mm/s ($Re = 0.025$). I_U and I_L represent the fluorescence intensities of the upper and lower half regions of 100 μm wide channel, respectively.

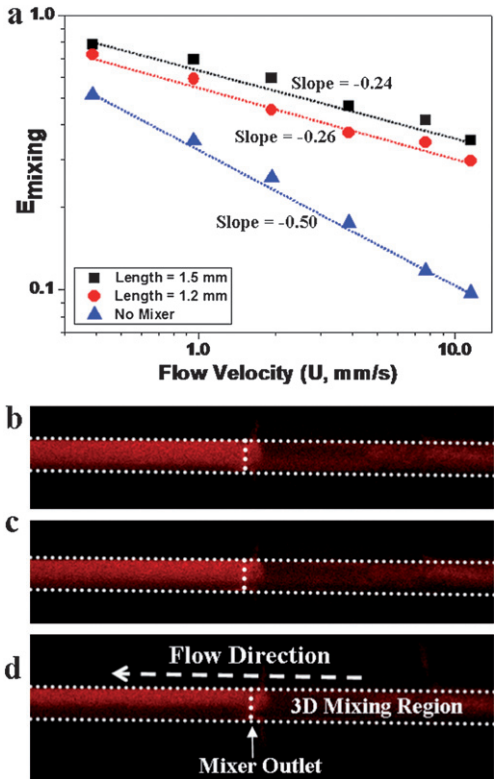

Fig. 7 Mixing efficiencies for different lengths. (a) The mixing efficiency of 3D mixers with different lengths of mixing units as a function of the flow velocity U, in log-log scale. The plots show that the data fit into the linear regression. Confocal microscopy images of 3D mixer $l = 1.5$ mm at the flow velocity of (b) 1.0 mm/s ($Re = 0.025$, $Pe = 6.9 \times 10^2$), (c) 1.9 mm/s ($Re = 0.05$, $Pe = 1.4 \times 10^3$), and (d) 7.7 mm/s ($Re = 0.2$, $Pe = 4.1 \times 10^3$). Vertical dotted lines indicate the outlet of the passive mixer.

efficiency for the 3D porous micromixer depended less strongly on the flow velocity than that for the "no mixer" system, as noted from Fig. 7a. For the 3D mixers of $l = 1.2$ and 1.5 mm, the power law behaved approximately as $-1/4$ power (or more accurately as -0.24 ± 0.02 and -0.26 ± 0.02, respectively) of U. The mixing efficiency for the 3D mixer of $l = 1.5$ mm was 20% higher than that observed for $l = 1.2$ mm.

As the flow velocity increased, the efficiencies of the 3D mixers dropped much more slowly than that of the "no mixer" system. Specifically, the degrees of mixing for the 3D mixer of $l = 1.2$ mm and the "no mixer" system were measured to be 0.72 ± 0.04 and 0.51 ± 0.03, respectively, at the flow velocity of 0.4 mm/s. When the flow velocity was increased to 1.9 mm/s, the mixing efficiencies of the 3D mixer and the "no mixer" system decreased to 0.45 ± 0.03 and 0.26 ± 0.006, respectively. At $U = 7.7$ mm/s, the mixing performance of the 3D mixer was 0.35 ± 0.03 and that for the "no mixer" system was approximately one third (0.12 ± 0.01). Because of flow splitting and recombination through the 3D interconnected open pores, the overall mixing efficiency of the system with a completely sealed mixing unit of 1.2 mm was 84% greater than that of the "no mixer" system with same length.

In Figs. 7b–7d, we reproduced confocal microscopy images of the 3D mixer of $l = 1.5$ mm at various Reynolds numbers (Re) and Peclet numbers ($Pe = l_c U/D$). The confocal images indicate clearly that the mixing efficiency was gradually decreased with increase in the flow velocity. As shown in Fig. 7d, the R6G dye molecules were dispersed in the opposite half-side at the outlet of the 3D mixer even when the flow velocity was increased to 7.7 mm/s for which $Re = 0.2$ and $Pe = 4.1 \times 10^3$. Compared with other types of passive micromixers, the flow splitting and recombination in the 3D pore network structures works favourably for $Re < 1$ and $Pe < 10^4$. In case of chaotic mixers, the mixing length required for 90% mixing efficiency at $Pe = 625$ and 2×10^3 was measured to be 3.5 mm and 7 mm, respectively.[6,8] The mixing efficiency through the 3D porous structures of $l = 1.5$ mm at $Pe = 686$ and 1.4×10^3 was measured to be 0.7 and 0.6, respectively. Also, our mixing length is much shorter than those of other simple passive mixers with parallel and serial serpentine channels.[2–5] This is due to the presence of highly compact substream channels in the 3D porous structures.[12]

Conclusions

We demonstrated a simple incorporation of micromixing units of 3D interconnected pore network inside a microfluidic channel by combining single prism holographic lithography and photolithography. The levelling between the 3D porous structures and the channel wall was greatly improved by using supercritical drying which induced negligible capillary force and reduced the internal stress within the 3D polymer network. Complete sealing of the microfluidic chip was achieved by preventing the volume shrinkage of the 3D structures and attaching a flexible PDMS cover substrate. Because the flow splitting and recombination was developed through the 3D interconnected pore network, a high mixing efficiency was achieved at low Re and low Pe regimes. The mixing performance of the system with the 3D mixing unit of $l = 1.2$ mm was 84% greater than that of the "no mixer" system of the same length. In addition to micromixers, the present 3D porous structures within a microfluidic channel can be used in the sorting and separation of DNAs and other biomolecules[26–28] and/or nanoparticles.[11]

Acknowledgements

This work was supported by a grant from the Creative Research Initiative Program of the MOST/KOSEF for "Complementary Hybridization of Optical and Fluidic Devices for Integrated Optofluidic Systems." The authors also appreciated partial support from the Brain Korea 21 Program. JHM thanks the support by the Sogang University Research Grant of 2008 and the Manpower Development Program for Energy & Resources supported by the Ministry of Knowledge and Economy (MKE).

References

1 N. T. Nguyen and Z. G. Wu, *J. Micromech. Microeng.*, 2005, **15**, R1–R16.
2 D. S. Kim, S. H. Lee, T. H. Kwon and C. H. Ahn, *Lab Chip*, 2005, **5**, 739–747.
3 B. He, B. J. Burke, X. Zhang, R. Zhang and F. E. Regnier, *Anal. Chem.*, 2001, **73**, 1942–1947.
4 A. A. S. Bhagat, E. T. K. Peterson and I. Papautsky, *J. Micromech. Microeng.*, 2007, **17**, 1017–1024.
5 F. G. Bessoth, A. J. deMello and A. Manz, *Anal. Commun.*, 1999, **36**, 213–215.

6 A. D. Stroock, S. K. W. Dertinger, A. Ajdari, I. Mezic, H. A. Stone and G. M. Whitesides, *Science*, 2002, **295**, 647–651.
7 H. Aref, *Phys. Fluids*, 2002, **14**, 1315–1325.
8 M. S. Williams, K. J. Longmuir and P. Yager, *Lab Chip*, 2008, **8**, 1121–1129.
9 D. Therriault, S. R. White and J. A. Lewis, *Nat. Mater.*, 2003, **2**, 265–271.
10 N. T. Nguyen and X. Y. Huang, *Lab Chip*, 2005, **5**, 1320–1326.
11 S. Jeon, J. U. Park, R. Cirelli, S. Yang, C. E. Heitzman, P. V. Braun, P. J. A. Kenis and J. A. Rogers, *Proc. Natl. Acad. Sci. U. S. A.*, 2004, **101**, 12428–12433.
12 S. Jeon, V. Malyarchuk, J. O. White and J. A. Rogers, *Nano Lett.*, 2005, **5**, 1351–1356.
13 G. H. Seong and R. M. Crooks, *J. Am. Chem. Soc.*, 2002, **124**, 13360–13361.
14 D. A. Mair, T. R. Schwei, T. S. Dinio, F. Svec and J. M. J. Frechet, *Lab Chip*, 2009, **9**, 877–883.
15 M. Campbell, D. N. Sharp, M. T. Harrison, R. G. Denning and A. J. Turberfield, *Nature*, 2000, **404**, 53–56.
16 L. J. Wu, Y. C. Zhong, C. T. Chan, K. S. Wong and G. P. Wang, *Appl. Phys. Lett.*, 2005, **86**, 241102.
17 S. K. Lee, S. G. Park, J. H. Moon and S. M. Yang, *Lab Chip*, 2008, **8**, 388–391.
18 J. H. Moon, J. Ford and S. Yang, *Polym. Adv. Technol.*, 2006, **17**, 83–93.
19 B. Li, M. Liu and Q. F. Chen, *J. Microlith. Microfab. Microsys.*, 2005, **4**, 043008.
20 T. Kondo, S. Juodkazis and H. Misawa, *Appl. Phys. A*, 2005, **81**, 1583–1586.
21 J. Q. Chen, W. Jiang, X. N. Chen, L. Wang, S. S. Zhang and R. T. Chen, *Appl. Phys. Lett.*, 2007, **90**, 093012.
22 H. Bruus, *Theoretical Microfluidics*, Oxford University Press Inc., New York, 2008, pp. 48–51.
23 T. Rohr, C. Yu, M. H. Davey, F. Svec and J. M. J. Frechet, *Electrophoresis*, 2001, **22**, 3959–3967.
24 R. F. Ismagilov, A. D. Stroock, P. J. A. Kenis, G. Whitesides and H. A. Stone, *Appl. Phys. Lett.*, 2000, **76**, 2376–2378.
25 J. B. Salmon and A. Ajdari, *J. Appl. Phys.*, 2007, **101**, 074902.
26 N. Pamme, *Lab Chip*, 2007, **7**, 1644–1659.
27 G. C. Randall, K. M. Schultz and P. S. Doyle, *Lab Chip*, 2006, **6**, 516–525.
28 L. R. Huang, J. O. Tegenfeldt, J. J. Kraeft, J. C. Sturm, R. H. Austin and E. C. Cox, *Nat. Biotechnol.*, 2002, **20**, 1048–1051.